BUTTERWORTH HEINEMANN

Measurement and prediction of natural convection velocities in triangular enclosures

Ronald D. Flack and Klaus Brun
Department of Mechanical, Aerospace, and Nuclear Engineering, University of Virginia, Charlottesville, VA, USA
Rita J. Schnipke
Blue Ridge Numerics, Inc., Charlottesville, VA, USA

Free convection velocities were predicted with a finite element method and measured using laser velocimetry in three isosceles triangular enclosures with base angles of 30°, 45°, and 60°. Three Grashof numbers were tested for each geometry, which ranged from 1.89×10^6 to 10.3×10^6. Velocity data were measured near the two isothermal side walls and the isothermal bottom wall. Data were nondimensionalized by the same parameters used to nondimensionalize inclined plate data. Flows were laminar for all cases. For a given base angle, the nondimensional data and predictions collapsed to single curves best for either of the side walls with typical variations of 5 percent; nondimensional predictions and data collapsed poorly for the bottom walls, with typical variations of 20 percent. Hot and cold side-wall data exhibited similitude and typical differences between nondimensional results for the two side walls were 10 percent. For varying base angles, side-wall results failed to reduce to single curves with variations of typically 50 percent. Absolute differences between predicted and measured peak velocities ranged from 6 to 35 percent. Differences between predicted and measured velocities for base angles of 30 and 60° tended to be positive, whereas, differences for a base angle of 45°, tended to be negative.

Keywords: natural convection; laminar flow; horizontal triangular enclosure; velocity measurement; isothermal surfaces

Introduction

Internal natural convection is important in many engineering applications. Electronic packaging, insulating voids, and solar panels are all devices in which heat transfer can dominate the effectiveness. Fire propensity is also an application in which low-speed natural convection can be an important factor.

Over the past years, heat transfer in a number of different geometries has been studied both experimentally and numerically. For example, natural convection in rectangular enclosures has been of interest for decades, and a number of the papers are identified in Ostrach (1988). More complex shapes have also been studied. For example, Flack et al. (1979), Flack (1980), Karyakin et al. (1988), del Campo et al. (1988), Akinsete and Coleman (1982), and Poulikakos and Bejan (1983) all studied the heat transfer in triangular enclosures. Next, Turner and Flack (1980) considered heat transfer in rectangular enclosures with concentrated temperature sources in the walls. These were direct electronic cooling applications. Lee and Goldstein (1988) experimentally studied heat transfer in a square enclosure with internal energy sources. Also, Lee (1984), Lam et al. (1989), and Peric (1993) studied free convection in nonrectangular trapezoidal enclosures. Finally, others have studied heat transfer in unconventional enclosures. For example, Abib and Jaluria (1988) predicted flows in partially open enclosures and Nansteel and Greif (1983) and Al-ani and Nansteel (1993) measured heat transfer in sector- shaped enclosures with partitions.

In all of the above, heat transfer was of primary importance. For many applications, effectively predicting heat transfer is the main concern. However, some applications are present in which the convection velocities are of equal or more importance. For example, over the past decade, fire hazard technology has received increased interest by both the government and industry. Fire propensity is directly related to induced air flows. These flows tend to increase the probability of fire ignition in housing and furniture applications because of an increased supply of oxygen. Yet, little data are available in the literature for velocity magnitudes or directions. Ozoe et al. (1983) and Lankhorst et al. (1993) accurately measured velocities; for both studies rectangular enclosures were of interest. Also, Giel and Schmidt (1990) and Schmidt et al. (1986) experimentally measured velocities for high Rayleigh number flows in rectangular enclosures.

Thus, the primary purpose of this paper is to present laser velocimetry data and theoretical predictions for the velocities in a triangular enclosure that has previously been studied for heat transfer correlations (Flack et al. 1979). The two sets of

Address reprint requests to Professor Flack at the Department of Mechanical, Aerospace, and Nuclear Engineering, University of Virginia, Thornton Hall, Charlottesville, VA 22903-2442 USA.

Received 9 April 1994; accepted August 1994

Int. J. Heat and Fluid Flow 16:106–113, 1995

655 Avenue of the Americas, New York, NY 10010

SSDI 0142-727X/95/$10.00
SSDI 0142-727X(94)00001-S

data complement each other. The data presented herein can be used to "benchmark" other prediction methods. Other purposes of the paper are to nondimensionalize the velocity profiles to examine for similitude for the data for the three walls, and to compare particularly the predicted and measured peak velocities, because the peak velocities lend themselves well to quantitative comparisons.

Test facility

Test rig

The air-filled enclosure consisted of three constant temperature water tanks (two sides and one bottom), as shown in Figure 1(a). The face of each side tank was polished aluminum (12.7 mm thick) and was 107.8 mm long, L by 254 mm wide, Z. The face of the bottom tank was also polished aluminum and was 254 mm wide. Six copper constantan thermocouples were embedded in each of the aluminum faces and were within 1.5 mm of the faces. The temperature of the plates were uniform to within 1°C. Radiation heat transfer to the air is less than 0.5 percent of the convection heat transfer for the worst case. For the cases presented in this paper, the side hot-water tank was connected using flexible hoses to a reservoir with electric heaters. A submersible pump in the reservoir was used to circulate the water. The side cold-water tank and the bottom tank were connected to a ice/water reservoir using hoses. Two submersible pumps were used to circulate the two flows.

Aluminum templates on both ends of the test section were screwed into the two side tanks and bottom tank for alignment. Adjustment of the apparatus to different geometries required only using different alignment holes in the templates. The end plates were made of 6.4 mm optical glass and were sealed on to the ends using silicon sealant. Seams around the corners of the enclosure were also sealed on the exterior using this sealant. In Flack et al. (1979), the heat transfer through the end plates was shown to be less than 5 percent of the heat transfer from the active surfaces. Three geometries were examined in this paper, and the idealized enclosure is presented in Figure 1(b). The values of W, H, θ_1, and θ_2 are listed in Table 1.

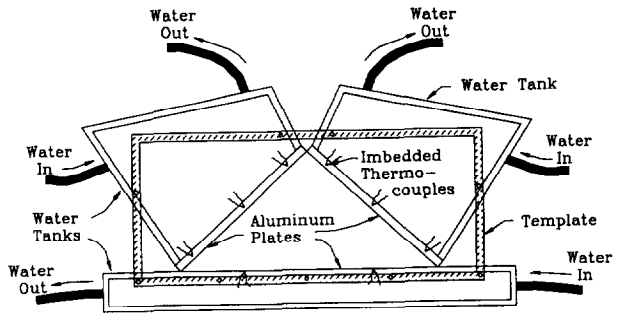

Figure 1(a) Enclosed rig schematic

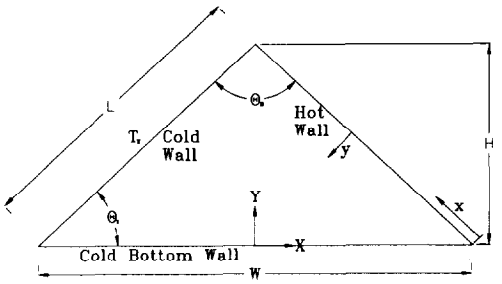

Figure 1(b) Ideal geometric boundaries

Table 1 Triangle geometries tested

W (mm)	H (mm)	W/H	θ_1 (deg)	θ_2 (deg)
107.8	93.3	0.865	60	60
152.4	76.2	0.500	45	90
186.7	53.9	0.289	30	120

Notation

c_p	constant pressure specific heat
g	gravitational acceleration
Gr	local Grashof number, $g\beta \cos(\theta_2/2)\,\Delta T L^3/\nu_r^2$
Gr′	overall Grashof number, $g\beta \cos(\theta_2/2)\Delta T' L^3/\nu_m^2$
H	triangle height, Figure 1
k	thermal conductivity
L	side length, Figure 1
p	pressure
p_{ref}	reference pressure
Pr	Prandtl number
$\mathscr{R}_{gas}$	gas constant
T	temperature
T_c	cold wall temperature
T_h	hot wall temperature
T_m	mean temperature, $(T_h + T_c)/2$
T_r	reference temperature, $T_w - 0.38\,(T_w - T_m)$
T_w	wall temperature
u	velocity in x- direction
U	nondimensional velocity, $(\mathrm{Gr}/4X)^{0.5}\, u\nu_r/g\beta \cos(\theta_2/2)\Delta T L^2$
v	velocity in y-direction
W	base width, Figure 1
x	direction parallel to wall, Figure 1
$\bar{x}$	nondimensional distance, x/L
X	Horizontal distance
y	direction normal to wall, Figure 1
$\bar{y}$	nondimensional distance, $\mathrm{Gr}^{0.25}\, y/L$
Y	Vertical distance
Z	axial length

Greek

β	volumetric coefficient of expansion, $1/T_m$
η	nondimensional distance, $\bar{y}/4\bar{x}^{0.25}$
θ_1	base angle, Figure 1
θ_2	apex angle, Figure 1
μ	dynamic viscosity
ν_m	kinematic viscosity at mean temperature
ν_r	kinematic viscosity at reference temperature
ρ	density
ΔT	local temperature difference, $T_w - T_m$
$\Delta T'$	overall temperature difference, $T_h - T_c$

Laser velocimeter

Laser velocimetry has been shown to be a effective and accurate method of measuring a wide range of velocity magnitudes. The technique has the advantage of reliably measuring multi-components of velocity without changing the characteristics of the flow.

The Argon–ion laser, data-processing units, and optics for the current system are shown in Figure 2. The system is three-color (511.5 nm, 488.0 nm, and 476.5 nm), six-beam, and frequency shifted; it is operated in the backscatter mode with fiber optics. The single laser beam is split into three beams with color separators and then split into the six beams using prisms. All six beams are focused and crossed at the probe volume measurement location); three sets of interference fringes are created. These three sets of fringes allow the simultaneous measurement of three independent components of velocity. Four beams are transmitted orthogonally by one optical probe and measure velocities in two orthogonal directions. The two remaining beams are transmitted with a different optical probe and measure a third independent direction. After the data are collected, three orthogonal directions of velocity are determined with vector transformations. The transmitting lenses have focal lengths of 600 mm. The effective size of the probe volume is approximately 0.15 mm in diameter and approximately 0.5 mm long. Bragg cells perform the function of frequency shifting by 40 MHz; this technique allows the measurement of flow reversals.

The entire optical system was mounted on a three-directional, computer-controlled, motor-driven traversing mechanism with digital position readouts. The probe volume was easily and accurately moved in the x, y, and z directions with this mechanism, with a positional accuracy of 80 μm over a range of 600 mm.

The frequency of light scattered from the interference fringes in the probe volume determines the velocity. Light was scattered by glucose/water particles that were 2 μm diameter. These particles were generated by an ultrasonic fogger and a mixture of 4 g of glucose to 100 ml of water. Scattered light was collected by the lenses in the optical probes and transmitted to photomultiplier tubes (PMTs) using fiber optics, where it was converted to electrical signals. Three frequency analysis-type signal processors were used to process the signals from the three PMTs. Signals from all three PMTs are checked for coincidence; namely, if all three signals occur at the same instant of time, they are considered valid. If the three signals do not occur at the same time, the signals are considered to be from different particles, and the data are discarded. The three valid velocity signals are finally recorded by a dedicated microcomputer.

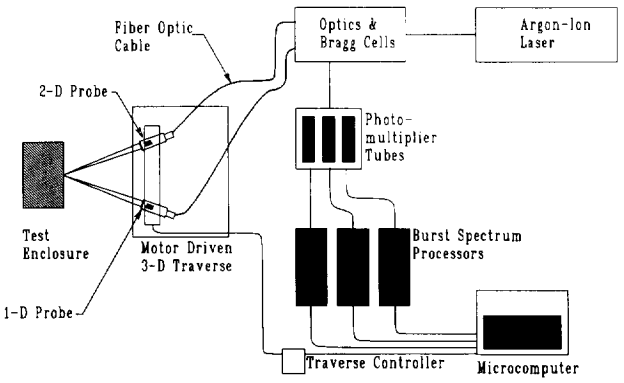

Figure 2 Block diagram of LV data system

Procedure

Each configuration was run at three different hot wall temperatures (20, 70, and 100°C); the cold walls were maintained at 0°C. The temperatures were controlled using current controllers on the electric heaters. After the rig reached steady temperatures, the seeding particles were injected into the enclosure, and the flow was allowed to stabilize for 30 min. Velocity measurements were taken along perpendicular traverses centrally located to the three walls. For example, for the hot wall velocities at $x_h/L = 0.5$ were measured. Thus, for each geometry, nine sets of data were collected. Only the velocity components parallel to the boundaries are reported in this paper.

Numerical method

The governing equations are the Navier–Stokes equations combined with the continuity equation, the thermal transport equation, and constitutive property relationships. The assumptions used in this analysis include: incompressible flow (Mach number < 0.3); two-dimensional (2-D), laminar flow; negligible radiation heat transfer effects; and constant fluid properties, except density, which varies inversely with temperature. With these assumptions, the governing equations reduce to the following:

$$\frac{\partial(\rho u)}{\partial X} + \frac{\partial(\rho v)}{\partial Y} = 0 \tag{1}$$

$$\frac{\partial(\rho uu)}{\partial X} + \frac{\partial(\rho uv)}{\partial Y} = -\frac{\partial p}{\partial X} + \mu\left(\frac{\partial^2 u}{\partial X^2} + \frac{\partial^2 u}{\partial Y^2}\right) \tag{2}$$

$$\frac{\partial(\rho uv)}{\partial X} + \frac{\partial(\rho vv)}{\partial Y} = -\frac{\partial p}{\partial Y} + \mu\left(\frac{\partial^2 v}{\partial X^2} + \frac{\partial^2 v}{\partial Y^2}\right) - \rho g \tag{3}$$

$$\frac{\partial(\rho u c_p T)}{\partial X} + \frac{\partial(\rho v c_p T)}{\partial Y} = k\left(\frac{\partial^2 T}{\partial X^2} + \frac{\partial^2 T}{\partial Y^2}\right) \tag{4}$$

$$\rho = \frac{p_{\text{ref}}}{\mathscr{R}_{\text{gas}} T} \tag{5}$$

with the variables defined in the Notation Box. For these equations, the viscosity and conductivity were evaluated at the average of the hot and cold wall temperatures. Both viscosity and conductivity were treated as constants in the analysis. Although they can vary as much as 10 percent over the temperature range considered in this paper, the overall effects of diffusion relative to advection are small, except at the lower velocities. Thus, the property variation may be more important at the lower Grashof numbers.

Because the goal of the analysis was to match the experimental data, the full Boussinesq approximation was not used. Allowing the density to vary nonlinearly with temperature more closely matches the actual physical phenomena that was measured. The dimensional equations were solved numerically to avoid any ambiguities caused by nondimensionalization parameters. The measured data were taken in dimensional space. The numerical data were produced likewise, so that the two could be compared from a common denominator.

The governing partial differential equations are discretized using the finite element method, specifically Galerkin's method of weighted residuals (Zienkiewicz 1977). The nonlinear advection or inertia terms are treated using a monotone streamline upwind method (Rice and Schnipke 1985). This method will produce only bounded solutions with a significant reduction in the numerical diffusion errors associated with the

conventional monotone upwind method. Schnipke (1986) contains a more complete discussion of the discretization method.

Equations 1 and 5 represent five equations in five unknowns. The discretized or algebraic form of these equations can be solved either simultaneously in one large matrix or in a segregated manner; i.e., one equation at a time. Because of the highly nonlinear nature of each of the governing equations, the segregated approach offers the most economic alternative. The segregated approach used here is based on the SIMPLER method (Patankar 1980). In this method, an explicit equation for pressure is derived by substituting a semidiscretized form of the momentum equations into the continuity equation. This pressure equation is solved in a sequential manner along with the two momentum equations and the thermal energy equation. This solution algorithm has proved to be quite robust and computationally efficient. Schnipke (1986) contains a more complete discussion of this algorithm.

Because of the nonlinear nature of the governing equations as well as the intimate coupling between the equations, a Picard iterative process is used to solve the equation set. The progress of the solution is monitored by observing the norm of the equation residuals. When the residual norm for each equation was below 10^{-5}, the solution was considered converged.

An unstructured finite element mesh with 3,596 nodes and 3,500 bilinear quadrilateral elements was used for most geometries. A finer mesh with 7,336 nodes and 7,200 quadrilateral elements was also used to check for mesh dependencies in the solution. The finer mesh yielded the same solution as the 3,596 node mesh for all cases, except the highest Grashof numbers with the triangular enclosure with $\theta_1 = 30°$. The numerical results presented are for the 3,596-node mesh, except for the 30° triangular enclosure at the highest Grashof number.

Results

General flow patterns

Most of the results herein are presented in the form of velocity profiles. Before presenting the details of the velocities, the general characteristics are presented in Figure 3. Both predicted streamlines and normalized isotherms are shown for the enclosure with $\theta_1 = 45°$ for an overall Grashof number Gr′ of 8.38×10^6. As can be seen, near the midpoint of the two side walls, a high-velocity gradient exists with a stagnant central region. At the midpoint of the lower wall, the velocity gradient is reduced. The isotherms indicate large thermal gradients near the side walls. At the midpoint of the lower wall, the isotherms are stratified.

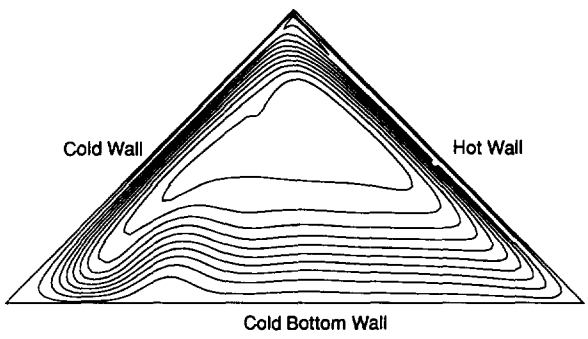

Figure 3(a) Predicted streamlines for $\theta_1 = 45°$ and Gr′ = 8.38×10^6

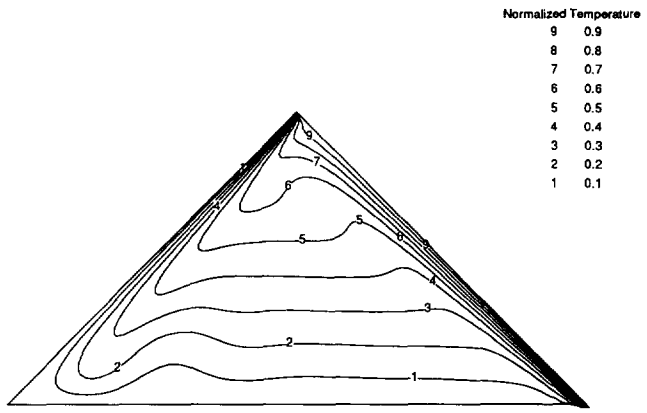

Figure 3(b) Predicted normalized isotherms for $\theta_1 = 45°$ and Gr′ = 8.38×10^6

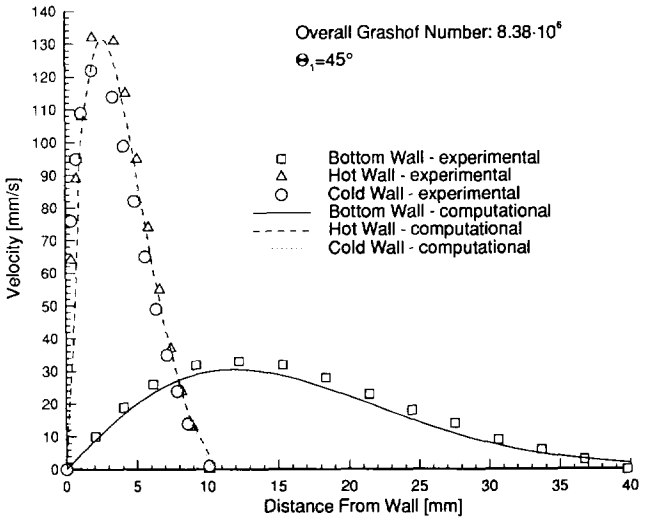

Figure 4 Velocity traverses from three walls for $\theta_1 = 45°$ and Gr′ = 8.38×10^6

Dimensional results

Nondimensionalization is used for most of the data and predictions presented herein. However, before proceeding, one set of dimensional results are presented in Figure 4. In this figure, the velocity components parallel to the three walls are presented for the traverses from the walls for the enclosure with $\theta_1 = 45°$ for an overall Grashof number Gr′ of 8.38×10^6. Both measurements and predictions are depicted. For this typical set of traverses, the perpendicular and axial components of velocity were at most 0.5 and 2 percent of the maximum value of velocity, respectively. Also, for this case and all other cases, the flow was laminar, and the fluctuations in velocity were at most 2 percent. Furthermore, in three-dimensional (3-D) numerical studies of similar triangular geometries, 3-D effects were not seen at the centerline of the geometry when the enclosure depth is three times the height of the triangle; variations in velocity and temperature were confined to within 10 percent of the ends. Thus, the centerline data for the geometry of interest represents 2-D flow.

The largest peak velocity is seen for the hot wall data, while the smallest peak velocity is seen for the bottom wall data. In general, the measured and predicted values of velocity are within 5 percent for all three walls.

Nondimensional results

With the concept of nondimensionalizing the profiles to a single curve, nine different schemes were attempted. The most successful nondimensionalization is for the parameters below, which is similar to that used for inclined flat plates by Kierkus (1968); namely, the velocity is reduced to the following:

$$U = (\mathrm{Gr}/4X)^{0.5}\, u\, \nu_r/g\, \beta \cos(\theta_2/2)\, \Delta T L^2. \quad (6)$$

where

$$\mathrm{Gr} = g\, \beta \cos(\theta_2/2)\, \Delta T L^3/\nu_r^2 \quad (7)$$

$$X = x/L \quad (8)$$

$$\beta = 1/T_m \quad (9)$$

$$\Delta T = T_w - T_m \quad (10)$$

$$T_m = (T_h + T_c)/2 \quad (11)$$

$$T_r = T_w - 0.38\,(T_w - T_m) \quad (12)$$

and the position is reduced to the following:

$$\eta = \bar{y}/4\bar{x}^{0.25} \quad (13)$$

where

$$\bar{y} = \mathrm{Gr}^{0.25}\, y/L \quad (14)$$

Thus, the hot wall data from Figure 4 ($\theta_1 = 45°$) and similar data for other Grashof numbers reduce to the data in Figure 5. As can be seen, the experimental nondimensional data do not exactly reduce to one curve for the three overall Grashof numbers. However, the nondimensional curves are within 17 percent of one another at the peak velocity. The theoretical nondimensional curves nearly collapse to a single curve and are within 7 percent of one another. The largest differences between the experimental data and predictions are for the lowest Grashof number, and at the peak velocity, the difference is 6 percent. The assumption of constant viscosity and conductivity will affect the results at the lowest Grashof numbers more significantly, because advection effects may not dominate diffusion here. For the other two Grashof numbers, the predicted velocities are lower than measured and result in small negative differences.

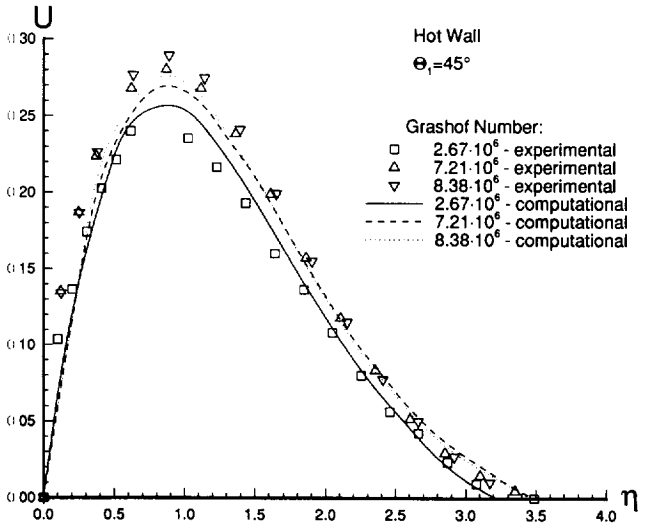

Figure 5 Nondimensional velocity traverses from hot wall for $\theta_1 = 45°$

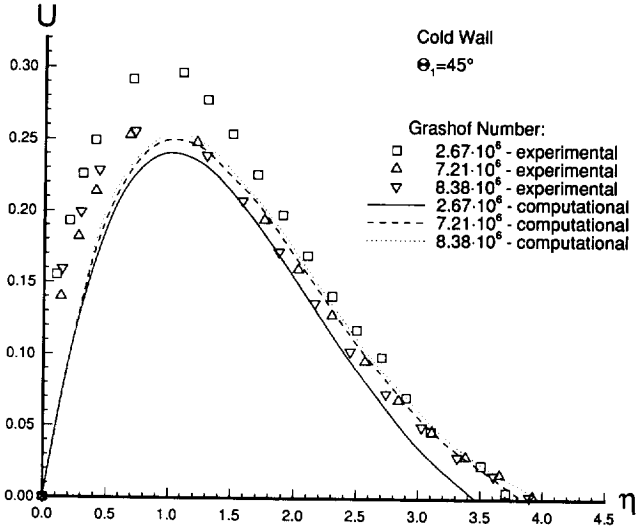

Figure 6 Nondimensional velocity traverses from side cold wall for $\theta_1 = 45°$

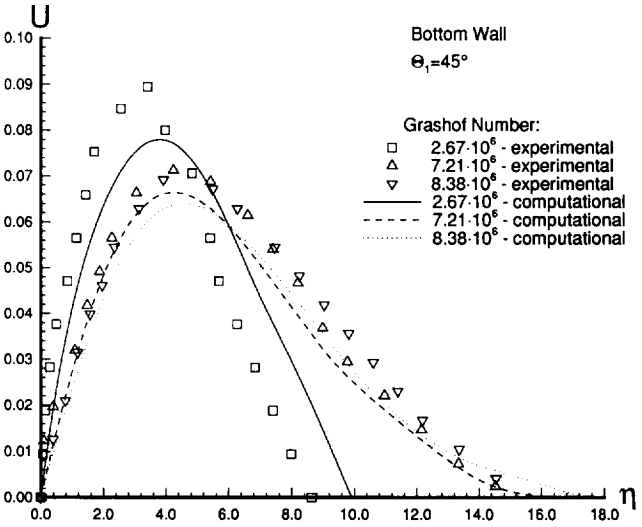

Figure 7 Nondimensional velocity traverses from bottom wall for $\theta_1 = 45°$

In Figure 6, the data for the cold wall for $\theta_1 = 45°$ are presented for three Grashof numbers. Nondimensional theoretical curves are within 6 percent of each other at the peak velocity. Experimental curves vary by 14 percent at the peak. The largest differences between the experimental data and predictions are for the lowest Grashof number, and at the peak velocity, the difference is -19 percent. Errors for the other two Grashof numbers are also negative.

Last, for $\theta_1 = 45°$, the data for the bottom wall are presented in Figure 7. For this wall, nondimensional theoretical curves are within 18 percent of each other at the peak velocity, which is a considerably higher difference than for the side walls. Experimental curves vary by 22 percent at the peak. The largest differences between the experimental data and predictions is, again, for the lowest Grashof number, and at the peak velocity, the difference is -13 percent. Errors for the other two Grashof numbers are also negative. In general, we would not expect the data for the bottom wall to collapse as well as for the side walls. Kierkus (1968) normalized his predictions so that the buoyancy

driving force was similar for different inclinations by modifying the Grashof number by the cosine of the inclination. However, for the current case, the horizontal bottom wall is not driving the flow as much as the side walls are. Also, data or predictions for flows over simple, cold horizontal plates do not demonstrate the same general tendencies as a vertical or inclined plate. Furthermore, the bottom wall velocities are primarily much smaller than the peak velocities, and so are the pressures. The iterative solvers used to calculate these velocities will be subject to some roundoff error. The lower velocities will be affected more than the higher values.

In Figure 8, three predictions are presented for $\theta_1 = 45°$, $Pr = 0.70$, and $Gr' = 8.38 \times 10^6$. The previously presented predictions for the two side walls and bottom wall are compared to the conventional velocity profile from a boundary-layer solution for a simple vertical or inclined plate (Kierkus 1968). As can be seen, the agreement between the velocity peaks near the side walls and inclined plate is best for the hot wall, with less than 1 percent difference. However, the difference in the peak velocity for the cold side wall and the inclined plate is 8 percent. Furthermore, the difference in the peak velocity for the bottom wall and the inclined plate is 79 percent. We can postulate that the entrainment process for the inclined plate is most similar to the hot wall. Thus, for the case and all other cases, the nondimensional profiles for the two side walls were similar, but both were much higher than for the bottom wall. From Figure 8 we also can see that the agreement between the width of the boundary layer velocity profile near the side walls and inclined plate is best for the cold wall.

Next, the hot wall data for $\theta_1 = 60°$ are presented in Figure 9. As for $\theta_1 = 45°$, the experimental nondimensional data do not exactly reduce to one curve for the three overall Grashof numbers; the nondimensional curves are within 18 percent of one another at the peak velocity. However, the predicted nondimensional curves nearly collapse to a single curve and are within 5 percent of one another. The largest differences between the experimental data and predictions are for the lowest Grashof number, and at the peak velocity the difference is 26 percent. Errors for the other two Grashof numbers are also positive.

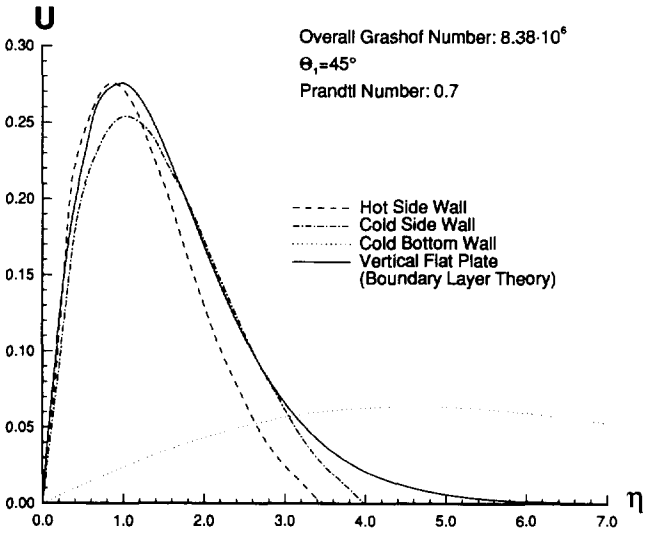

Figure 8 Three predicted nondimensional velocity profiles from side walls and bottom wall for $\theta_1 = 45°$ and $Gr' = 8.38 \times 10^6$

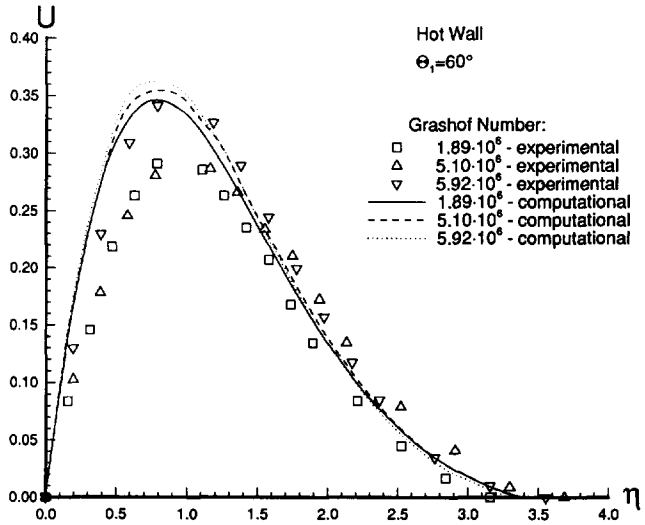

Figure 9 Nondimensional velocity traverses from hot wall for $\theta_1 = 60°$

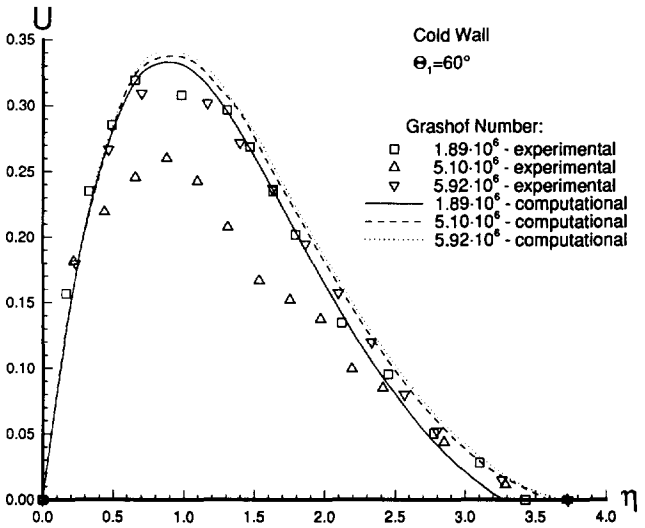

Figure 10 Nondimensional velocity traverses from side cold wall for $\theta_1 = 60°$

In Figure 10, the data for the cold wall for $\theta_1 = 60°$ are presented for three Grashof numbers. Predicted theoretical curves are within 3 percent of each other at the peak velocity. Experimental curves vary by 23 percent at the peak. The largest differences between the experimental data and predictions are for the intermediate Grashof number, and at the peak velocity, the difference is 35 percent. Errors for the other two Grashof numbers are also positive.

Last, the data for the bottom wall are presented in Figure 11 for $\theta_1 = 60°$. The predicted nondimensional curves are within 16 percent of each other at the peak velocity, which again is considerably higher than for the side walls. Experimental curves vary by 29 percent at the peak. The largest differences between the experimental data and predictions is for the largest Grashof number, and at the peak velocity, the difference is 15 percent. Errors for the other two Grashof numbers are negative.

The hot wall data for $\theta_1 = 30°$ are presented in Figure 12. As for the other values of θ_1, the experimental nondimensional

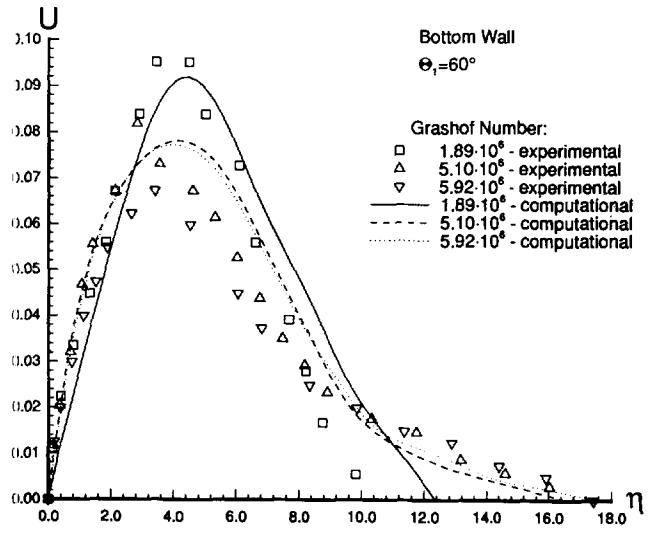

Figure 11 Nondimensional velocity traverses from bottom wall for $\theta_1 = 60°$

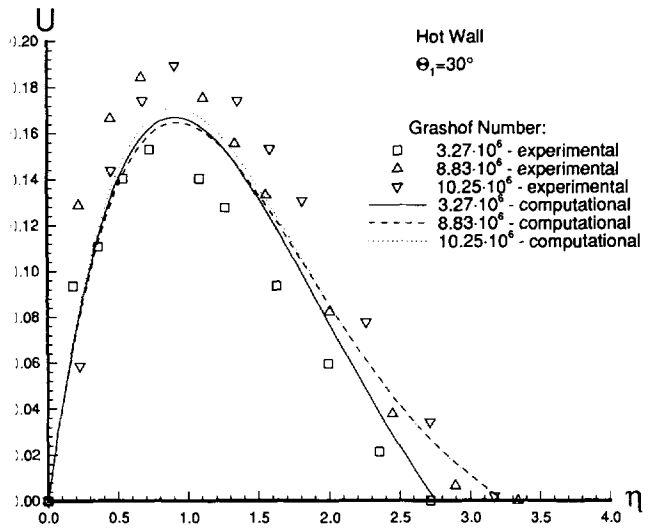

Figure 12 Nondimensional velocity traverses from hot wall for $\theta_1 = 30°$

data do not exactly reduce to a single curve for the three overall Grashof numbers. For these data, the nondimensional curves are within 19 percent of one another at the peak velocity. The theoretical nondimensional curves are within 4 percent of one another. The largest differences between the experimental data and predictions are for the largest Grashof number, and at the peak velocity, the difference is 17 percent. Errors for the other two Grashof numbers are negative.

In Figure 13, the data for the cold wall for $\theta_1 = 30°$ are presented. Predicted nondimensional curves are within 4 percent of each other at the peak velocity. Experimental curves also vary by only 4 percent at the peak. The differences between the experimental data and predictions at the peak velocity are the same for all Grashof numbers, and the difference is 9 percent.

Finally, the data for the bottom wall for $\theta_1 = 30°$ are presented in Figure 14. The predicted nondimensional curves are within 20 percent of each other at the peak velocity, which again, is considerably higher than for the side walls. Experimental curves vary by 35 percent at the peak. The largest differences between the experimental data and predictions is for the smallest Grashof number, and at the peak velocity, the differences is −20 percent. The errors for the largest and intermediate Grashof numbers are both positive.

A finer mesh was necessary for the triangular enclosure with $\theta_1 = 30°$ at the highest Grashof number than for the other geometries. We should note that the Grashof number increases as the apex angle of the triangle increases. Hence, for a given temperature difference, the 30° triangular enclosure has the highest Grashof numbers, and, therefore, exhibits the least stable physical flow regime. The numerical solution reflected this decreased stability and required a finer mesh to determine an accurate solution. From these results, we conclude that the finer mesh is required for Grashof numbers greater than 10^7.

Last, we can compare the nondimensional profiles for the different geometries. For example, by comparing Figures 5, 9, and 12, the dependence on θ_1 can be ascertained. Ideally, for an inclined plate, the dependence is minimal because the gravity term in the Grashof number is "corrected" (Kierkus 1968).

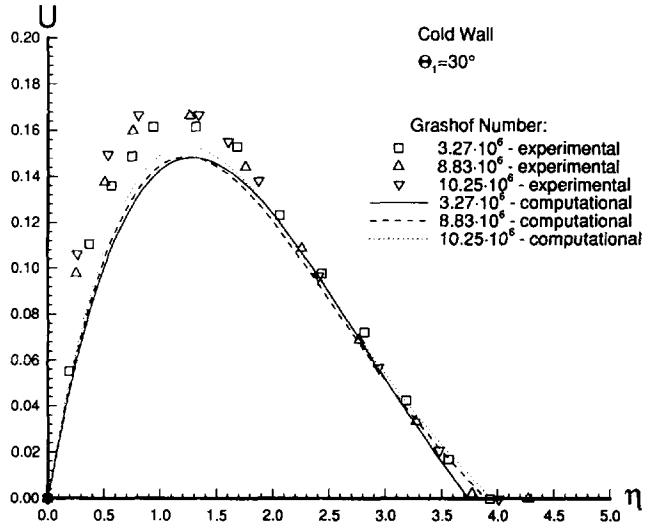

Figure 13 Nondimensional velocity traverses from side cold wall for $\theta_1 = 30°$

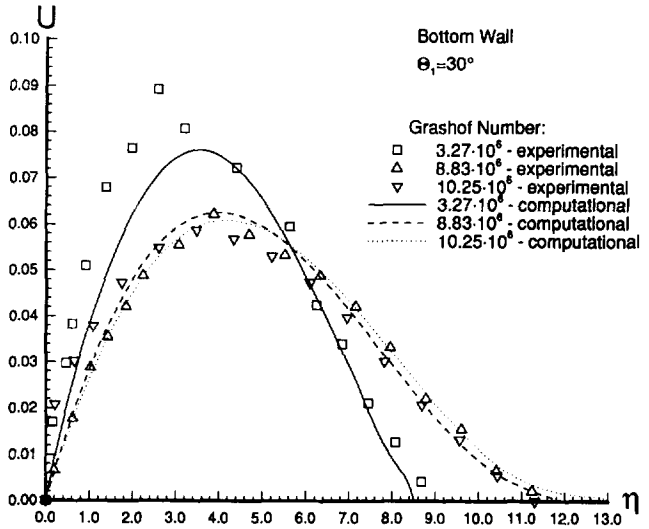

Figure 14 Nondimensional velocity traverses from bottom wall for $\theta_1 = 30°$

However, the predictions of the peak velocity near the hot wall vary from 0.35 to 0.27 to 0.17, as θ_1 is decreased from 60 to 45 to 30°. Similarly, the predictions of the peak velocity near the cold side wall (Figures 6, 10, and 13) vary from 0.34 to 0.25 to 0.15 as θ_1 is decreased from 60 to 45 to 30°. Thus, because of the complex interaction of the walls, typical variations are 50 percent for this range of θ_1.

Conclusions

Free-convection velocities were predicted and measured in three isosceles triangular enclosures; base angles were 30, 45, and 60°. Temperatures were varied, and three Grashof numbers (over a relatively limited range) were tested for each geometry. Velocity data were measured using laser velocimetry near the two isothermal side walls and the isothermal bottom wall. Predictions of the flowfield were made using a finite element method. Data were nondimensionalized by the same parameters used to nondimensionalize inclined plate data. Specific conclusions are as follows.

(1) Flows were laminar for all cases. Velocity fluctuations were less than 2 percent.
(2) For a given geometry, but varying Grashof numbers, both the nondimensional data and predictions collapsed to single curves best for either of the side walls. Variations in the peaks of the predicted curves were 3 to 7 percent for a given base angle and given side wall. Experimental peak data varied from 14 to 23 percent for these cases.
(3) Nondimensional predictions and data for a given geometry collapsed poorly for the bottom walls. Differences in peaks ranged from 16 to 20 percent for the predictions and 22 to 35 percent for the experimental data. For the bottom walls, the buoyancy forces are of different character than for the inclined side walls.
(4) For a given geometry and given Grashof number, the nondimensional results for both side walls exhibited similitude; typical differences of the peak velocities of the hot and cold walls were 10 percent. However, the peak velocity results for the bottom wall were typically 80 percent different than those from the side walls.
(5) For varying geometries, neither the nondimensional data nor predictions collapsed to single curves, in spite of the gravity correction used in the nondimensionalization. Typical variations of the peak velocities were 50 percent as the base angle was varied.
(6) Absolute differences between predicted and measured velocities ranged from 6 to 35 percent. Errors for base angles of 30 and 60° tended to be positive; whereas, errors for a base angle of 45° tended to be negative.

Acknowledgments

The authors and the University of Virginia express their appreciation for a grant by the Cigarette Ignition Propensity Research Joint Venture to support this research partially. The research was also partially supported by the Rotating Machinery and Controls Laboratory at the University of Virginia and by Blue Ridge Numerics, Inc.

References

Abib, A. H. and Jaluria, Y. 1988. Numerical simulation of the buoyancy induced flow in a partially open enclosure. *Num. Heat Transfer*, **14**, 235–254

Akinsete, V. A. and Coleman, T. A. 1982. Heat transfer by steady laminar free convection in triangular enclosures. *Int. J. Heat Mass Transfer*, **25**, 991–998

Al-ani, N. and Nansteel, M. W. 1993. Natural convection in a partial sector-shaped enclosure: Experimental results. *J. Heat Transfer*, **115**, 133–139

del Campo, E. M., Sen M. and Ramos, E. 1988. Analysis of laminar natural convection in a triangular enclosure. *Num. Heat Transfer*, **13**, 353–372

Flack, R. D., Konopnicki, T. T. and Rooke, J. H. 1979. The measurement of natural convective heat transfer in triangular enclosures. *J. Heat Transfer*, **101**, 648–654

Flack, R. D. 1980. The experimental measurement of natural convection heat transfer in triangular enclosures heated or cooled from below. *J. Heat Transfer*, **102**, 770–772

Giel, P. W. and Schmidt, F. W. 1990. Comparison of turbulence modeling predictions to experimental measurements for high Rayleigh number natural convection in enclosures. *Proc. Ninth Int. Heat Transfer Conf.*, Jerusalem, Israel, Paper 2-NC-03, 175–180

Karyakin, Y. E., Sokovishin, Y. A. and Martynenko, O. G. 1988. Transient natural convection in triangular enclosures. *Int. J. Heat Mass Transfer*, **31**, 1759–1766

Kierkus, W. T. 1968. An analysis of laminar free convection flow and heat transfer about an inclined isothermal plate. *Int. J. Heat Mass Transfer*, **11**, 241–253

Lam, S. W., Gani, R. and Symons, J. G. 1989. Experimental and numerical studies of natural convection in trapezoidal cavities. *J. Heat Transfer*, **111**, 372–377

Lankhorst, A. M., Angirasa, D. and Hoogendoorn, C. J. 1993. LDV measurements of buoyancy-induced flows in an enclosure at high Rayleigh numbers. *Exp. Thermal Fluid Sci.*, **6**, 74–79

Lee, T. S. 1984. Computational and experimental studies of convective fluid motion and heat transfer in inclined non-rectangular enclosures. *Int. J. Heat Fluid Flow*, **5**, 29–36

Lee, J. H. and Goldstein, R. J. 1988. An experimental study on natural convection heat transfer in an inclined square enclosure containing internal energy sources. *J. Heat Transfer*, **110**, 345–349

Nansteel, M. W. and Greif, R. 1983. Natural convection heat transfer in complex enclosures at large Prandtl number. *J. Heat Transfer*, **105**, 912–915

Ostrach, S. 1988. Natural convection in enclosures. *J. Heat Transfer*, **110**, 1175–1190

Ozoe, H., Ohmuro, M., Mouri, A., Mishima, S., Sayama, H. and Churchill, S. W. 1983. Laser-doppler measurements of the velocity along a heated vertical wall of a rectangular enclosure. *J. Heat Transfer*, **105**, 782–788

Patankar, S. V. 1980. *Numerical Heat Transfer and Fluid Flow*, Hemisphere, New York

Peric, M. 1993. Natural convection in trapezoidal enclosures. *Num. Heat Transfer*, **24A**, 213–219

Poulikakos, D. and Bejan, A. 1983. Natural convection experiments in a triangular enclosure. *J. Heat Transfer*, **105**, 652–655

Rice, J. G. and Schnipke, R. J. 1985. A monotone streamline upwind finite element method for convection-dominated flows. *Comp. Methods Appl. Mech. Eng.*, **48**, 313–327

Schmidt, F. W., Giel, P. W., Phillips, R. E. and Wang, D. F. 1986. A comparison of experimental and predicted results for laminar natural convection in an enclosure. *Int. J. Heat Fluid Flow*, **7**, 183–190

Schnipke, R. J. 1986. A streamline upwind finite element method for laminar and turbulent flow, Ph.D. dissertation, University of Virginia, Charlottesville, VA

Turner, B. L. and Flack, R. D. 1980. The experimental measurement of natural convective heat transfer in rectangular enclosures with concentrated energy sources. *J. Heat Transfer*, **102**, 236–241

Zienkiewicz, O. C. 1977. *The Finite Element Method*, McGraw-Hill, New York